This is an author-created version of an article published in
ACS Applied Nanomaterials, 2, 5108–5115 (2019)
DOI: 10.1021/acsanm.9b01006. ©2019 American Chemical Society.

The Version of Record is available online at https://doi.org/10.1021/acsanm.9b01006 .

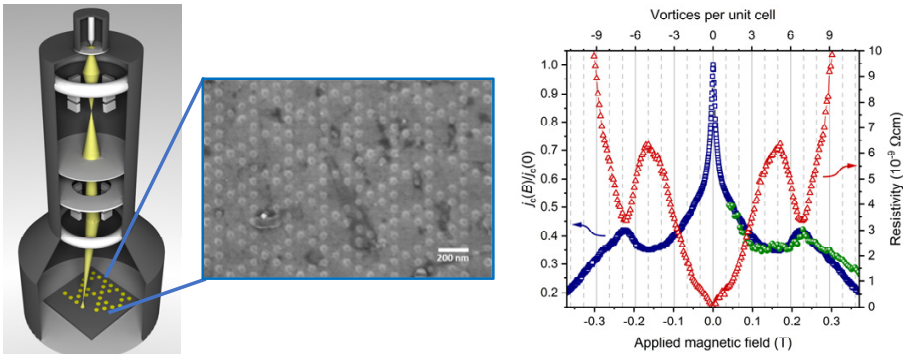
arXiv:1905.09070v2 [cond-mat.supr-con] 27 Aug 2019

Ultradense Tailored Vortex Pinning Arrays in Superconducting $YBa_2Cu_3O_{7-\delta}$ Thin Films Created by Focused He Ion-Beam Irradiation for Fluxonics Applications

Bernd Aichner,[†] Benedikt Müller,[‡] Max Karrer,[‡] Vyacheslav R. Misko,[¶,§,‖] Fabienne Limberger,[‡] Kristijan L. Mletschnig,[†] Meirzhan Dosmailov,[⊥] Johannes D. Pedarnig,[⊥] Franco Nori,[§,#] Reinhold Kleiner,[‡] Dieter Koelle,[‡] and Wolfgang Lang*[,†]

†*Faculty of Physics, University of Vienna, Wien, Austria*
‡*Physikalisches Institut and Center for Quantum Science (CQ) in LISA⁺, Universität Tübingen, Tübingen, Germany*
¶*Department of Physics, Universiteit Antwerpen, Antwerpen, Belgium*
§*Theoretical Quantum Physics Laboratory, RIKEN Cluster for Pioneering Research, Wako-shi, Saitama, Japan*
‖*μFlow group, Department of Chemical Engineering, Vrije Universiteit Brussel, Brussels, Belgium*
⊥*Institute of Applied Physics, Johannes Kepler University Linz, Linz, Austria*
#*Physics Department, University of Michigan, Ann Arbor, USA*

E-mail: wolfgang.lang@univie.ac.at



ABSTRACT: Magnetic fields penetrate a type II superconductor as magnetic flux quanta, called vortices. In a clean superconductor they arrange in a hexagonal lattice, while by addition of periodic artificial pinning centers many other arrangements can be realized. Using the focused beam of a helium ion microscope we have fabricated periodic patterns of dense pinning centers with spacings as small as 70 nm in thin films of the cuprate superconductor $YBa_2Cu_3O_{7-\delta}$. In these ultradense kagomé-like patterns, the voids lead to magnetic caging of vortices, resulting in unconventional commensurability effects that manifest themselves as peaks in the critical current and minima in the resistance versus applied magnetic field up to ~ 0.4 T. The various vortex patterns at different magnetic fields are analyzed by molecular-dynamics simulations of vortex motion, and the magnetic field dependence of the critical current is confirmed. These findings open the way for a controlled manipulation of vortices in cuprate superconductors by artificial sub-100 nm pinning landscapes.
KEYWORDS: *helium ion microscope, cuprate superconductor, vortex pinning lattice, commensurability effects, critical current*

1 INTRODUCTION

Superconductivity is one of the most intriguing phenomena in condensed matter physics and in particular the cuprate superconductors pose a challenge to the understanding of their electron-pairing mechanism. Still, their high transition temperature T_c and their possible high operating temperature in the accessible range of reliable and easy-to-handle cryocooler technology, make the cuprate superconductors primary candidates for emerging technologies. However, all superconductors are only marginally suitable for technical applications in their pure and clean form. It is by the introduction of controlled defects that superconductors can be tailored for many important properties, e.g., by enhancing their ability to carry a lossless current, which requires to impede the dissipative motion of magnetic flux quanta, also called Abrikosov vortices or fluxons.[1]

Whereas such enhanced vortex pinning in conventional metallic superconductors, typically used for medical applications and high-field magnets, has been achieved by metallurgical techniques, the brittle nature of cuprate high-T_c superconductors (HTSCs) requires different concepts. A successful approach is to create columnar amorphous regions with diameters of a few times the superconducting coherence length by irradiation with swift heavy ions.[2]

In contrast to these extended defects, point defects can be created by inclusion of tiny non-superconducting particles,[3] or by electron, proton, and light ion irradiation of HTSCs. For energies up to few megaelectronvolts the incident particles collide with a nucleus and displace it, eventually creating a collision cascade for high enough recoil energies. Several studies[4–6] have revealed that irradiation with He^+ ions of moderate energy is well suitable to tailor the superconducting properties in thin films of the prototypical HTSC $YBa_2Cu_3O_{7-\delta}$ (YBCO) by displacing mainly oxygen atoms, leading to a controllable reduction or even complete suppression of T_c. Arrays of cylindrical defect channels (CDs) that are populated with point defects provide a landscape in which superconductivity is locally suppressed. Recently, it has been demonstrated[7–14] that such pinning potential landscapes allow one to accommodate vortices in a commensurate arrangement, leading to peaks in the critical current and minima of the resistance at well-defined matching magnetic fields.

In the field of vortex commensurability effects, a large body of research has been established for metallic superconductors, typically using an array of holes (antidots) or blind holes with about 1 μm spacings.[15] Considerably narrower spacings have been achieved for thin Nb films grown on porous substrates.[16,17] However, in these superconductors, the Ginzburg–Landau coherence length at zero temperature is on the order of $\xi(0) \sim 10$ nm and the London penetration depth on the order of $\lambda_L(0) \sim 100$ nm, the latter setting the range of magnetic interaction between vortices. Commensurability effects could be explored only at temperatures T very close to T_c, taking advantage of the fact that $\lambda_L(T) = \lambda_L(0)[T_c/(T_c - T)]^{1/2}$ increases substantially when approaching T_c. But choosing a rather high operation temperature is not feasible for practical applications since it is on the expense of a reduced superconducting gap, weaker pinning potential, and enhanced thermodynamic fluctuations.

On the other hand, thin films of YBCO have an in-plane $\lambda_{L,ab}(0) \sim 250$ nm,[18–21] and edge and screw dislocations, as one important type of intrinsic defects in YBCO films, have typical distances of about 300 nm.[22] Still, commensurability effects could be demonstrated close to T_c in YBCO perforated with a square array of holes with 1 μm lattice spacing.[23] But since intrinsic defects compete with the artificially created pinning landscape, it is important to fabricate and investigate pinning arrays with lattice spacings significantly below these two characteristic lengths. Here, we report on the electrical transport properties of ultradense unconventional pinning arrays in YBCO thin films with spacings down to 70 nm, fabricated with a helium ion microscope, and we demonstrate pronounced commensurability effects at strong magnetic fields well above 100 mT which persist down to at least ~ 50 K, i.e., far below T_c.

2 RESULTS AND DISCUSSION

2.1 Irradiation in the Helium Ion Microscope. The ZEISS ORION NanoFab[24] is a novel multifunctional platform combining focused ion beam sources for neon and helium ions and a scanning helium ion microscope (HIM) with a spatial resolution better than 0.5 nm and unprecedented depth of focus.[25–27] The HIM consists of a gas-field He^+ ion source that emits ions from an ultrasharp tip, electrostatic ion optics to focus and trim the beam, and a deflection system to raster the beam over the sample stage as it is outlined in Figure 1a. The advantage of using a He beam over the conventional Ga focused ion beam technique is its higher spatial resolution (fabrication of nanopores down to 1.3 nm has been demonstrated[28]) and the prevention of contamination of the HTSC by Ga ions. As a first application in YBCO, the fabrication of Josephson junctions and superconducting quantum interference devices has been demonstrated via forming thin barriers of insulating material with the focused ion beam across prepatterned microbridges.[29–32]

However, for the fabrication of vortex pinning defects, the HIM in its original operation mode is less suitable. On the one hand, it is known that the diameter of defects suitable for vortex pinning must not be smaller than the superconducting coherence length, which is $\xi_{ab}(0) \simeq 1.2\,\mathrm{nm}$ in YBCO.[33] On the other hand, the inherent deflection of the ion trajectories by scattering at the target atoms when traversing the material will cause a blurring of the focus with increasing depth. In this situation the fluence of the He^+ ions decreases strongly from the surface to the back of the YBCO film. To achieve a high enough ion fluence for suppression of T_c throughout the entire film thickness, the intensity of the focused ion beam must then be set to such a high value that amorphization of the YBCO crystal lattice[7,32] and mechanical destruction near the sample's surface result. This is illustrated in Figure 1b which was recorded in the HIM after irradiation of a test pattern with an optimally focused He^+ ion beam with a much larger number of ions/spot than normally used in our experiments. Around the impact point of the focused ion beam the YBCO structure is completely destroyed and blisters with about 50 nm diameter bulge out of the surface, while under the regular conditions for fabrication of pinning lattices, the irradiated areas are invisible in both the HIM and with scanning electron microscopy.

To avoid these shortcomings and irradiate a well-defined area, our approach uses an intentionally defocused ion beam. This is achieved by first adjusting the HIM settings to highest resolution and afterward changing the working distance (beam focus plane) by 8 μm. The aperture angle of the ion beam is $\pm 0.07°$; hence, the ion beam hits the sample surface almost orthogonally with a nearly Gaussian fluence profile[28] with a full width at half maximum (fwhm) of about 20 nm.

The resulting three-dimensional shape of CDs with suppressed T_c is inferred from simulations of ion–matter interaction and collision cascades with the program SRIM[34] and calibrated to experimental data of T_c suppression as a function of defect density. Details of such calculations are reported elsewhere.[35] A defocused 30 keV He^+ beam of 20 nm fwhm diameter creates well-defined cylindrical channels with diameters $\sim 25\,\mathrm{nm}$ in a YBCO film within which T_c is suppressed or reduced up to a depth of 80 nm, as evidenced in Figure 1c. In thicker YBCO films, however, the collision cascades are prone to substantial straggling which leads to blurring of the profile and insufficient reduction of T_c due to a lower defect density as it has been observed in heavy–ion–irradiated YBCO single crystals.[36]

2.2 Vortex Commensurability Effects in Quasi-Kagomé Vortex Pinning Arrays. As a proof-of-concept experiment we have fabricated a square array of columnar defect cylinders with a defocused ion beam of fwhm = 50 nm and with a lattice spacing (nearest–neighbor distance) $a = 200\,\mathrm{nm}$ in a 80 nm thick YBCO film and measured the critical current $I_c(B_a)$ in the superconducting state and the magnetoresistance $R(B_a)$ in the voltage state as a function of the applied magnetic field B_a. The parameters were chosen similarly to previous experiments performed with masked ion beam irradiation.[10–13]

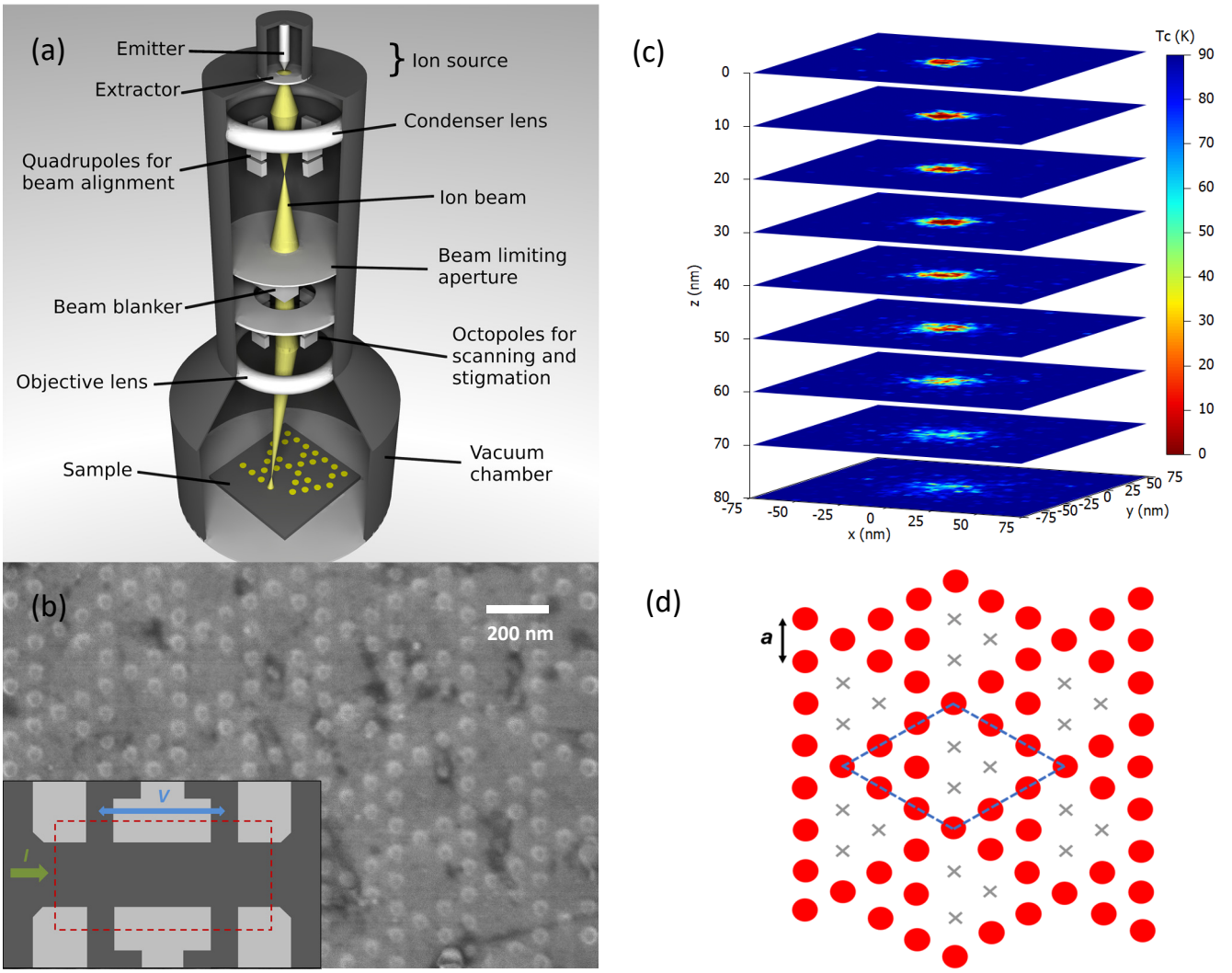


Figure 1: (a) Schematic drawing of direct modification of the local superconducting properties in a HIM. (b) HIM image of a quasi-kagomé test pattern of HIM-induced defects in a YBCO film, irradiated with a fully focused beam and with 5×10^6 ions/spot, i.e., with a 333 times larger number than in (c). The lattice spacing is $a = 90\,\mathrm{nm}$. Inset: sketch of the YBCO thin film samples (dark gray), the $200\,\mu\mathrm{m} \times 100\,\mu\mathrm{m}$ rectangular irradiated area (red broken lines), direction of the applied current I, and the voltage probes V. (c) Simulation of defect-induced spatial distribution of T_c of a YBCO film (within sheets at various depths z from the surface $z = 0$), upon irradiating one spot with a defocused 30 keV He^+ ion beam with a Gaussian normal distributed fluence of 20 nm fwhm diameter. The number of impacting ions (15000) is the same as in the experiments (per spot) and corresponds to an average fluence of $4.8 \times 10^{15}\,\mathrm{cm}^{-2}$. (d) Sketch of the pinning lattice with lattice spacing a: red disks represent irradiated spots, the blue dashed lines indicate the unit cell of the quasi-kagomé tiling, and gray crosses mark those sites that were removed from the hexagonal lattice to form the quasi-kagomé tiling.

Consistently, a clear peak of $I_c(B_a)$ corresponding to a minimum of $R(B_a)$ is found when each CD is filled by one vortex, and a tiny feature can be noticed for filling of each CD by two vortices (see the Supporting Information).

Pinning lattices can be designed not only with common hexagonal[37] or square tilings[15] but also as more complex periodic or even quasi-periodic tilings that exhibit a number of unusual phenomena. Some examples of such arrays have been studied theoretically[38–41] and experimentally in metallic superconductors

with holes[42–44] and magnetic dots,[45–48] like Penrose,[42,43] honeycomb[16,49] and kagomé[50] lattices and artificial vortex ice arrangements in geometrically frustrated pinning lattices.[51–53] In HTSCs, such studies have been scarce[54] due to the much more demanding nanopatterning.

The particular advantage of irradiation in the HIM over other nanopatterning techniques is the higher spatial resolution and the ability to easily produce any desired pattern. We demonstrate this by the fabrication of quasi-kagomé pinning lattices with ultrasmall lattice spacing $a = 90\,\mathrm{nm}$ (sample QK90) and 70 nm (sample QK70). The quasi-kagomé lattice is formed from a hexagonal lattice, where three neighboring sites are not occupied,[48] as sketched in Figure 1d. The quasi-kagomé lattice consists of vertex triangles with six sites per unit cell and large voids. It provides a unique platform to investigate the competition between pinning potentials and elastic energy of the vortex lattice. The quasi-kagomé lattice is a more extreme variant of the genuine kagomé tiling, which is formed from the hexagonal lattice by eliminating every other site from every other row.

In periodic pinning lattices commensurability effects are expected to occur at applied magnetic fields that fulfill the matching condition

$$B_k = \frac{k\Phi_0}{A} \tag{1}$$

where k is the number of pinning sites (or vortices) in the unit cell of area A and $\Phi_0 = h/(2e)$ is the magnetic flux quantum.

The electrical transport properties of the YBCO films patterned with the quasi-kagomé pinning lattice show intriguing features. Those can be attributed to the fact that HIM nanopatterning enables the realization of ultradense pinning arrays. Accordingly, pronounced vortex commensurability effects in the critical current density $j_c(B_a)$ and the magnetoresistivity $\rho(B_a)$ appear at very high matching fields, at $B_a = 0.23\,\mathrm{T}$ for sample QK90 and at $B_a = 0.38\,\mathrm{T}$ for sample QK70, as shown in Figures 2a and 2b, respectively. The observed effects are well reproducible after storing the samples at room temperature for several weeks.

In the case of strong interactions between vortices and the pinning potential of the CDs, significant vortex commensurability effects are expected at B_6, when each CD is filled with one vortex. Conversely, with strong vortex–vortex interactions and marginal influence of the pinning landscape, the elastic energy of the vortex ensemble should favor a hexagonal lattice and the voids are expected to be filled with three interstitial vortices, leading to commensurability signatures at B_9. The former, for instance, was observed in a quasi-kagomé lattice of magnetic Ni dots embedded in a Nb superconducting film.[48]

Surprisingly, none of these features are found here; instead, a prominent matching peak in $j_c(B_a)$ and a corresponding minimum in $\rho(B_a)$ appear at B_7, as can be seen in Figure 2a,b. Presumably, all CDs are occupied by vortices and one interstitial vortex per unit cell is "caged" inside the voids of the lattice due to repulsion forces from the trapped vortices. On the other hand, the absence of a matching feature at B_1 indicates that the six closely packed sites of the kagomé triangle do not merge into a single pinning site. This confirms that despite the rather narrow distance of CDs they act as separate pinning potentials.

Molecular dynamics simulations shed more light on the vortex distribution in the quasi-kagomé lattice. A rectangular cell with periodic boundary conditions is used for the calculations. The vortex–vortex interaction, the pinning force on the vortices at the CDs, an external driving force, and a thermal stochastic force are taken into account, as detailed elsewhere for previous simulations.[39,40,55,56] The ground state of the static vortex arrangement (zero driving force) is obtained by starting the simulation at some elevated "temperature" and gradually decreasing it to zero, thus performing a simulated thermal annealing. Note that this corresponds to magnetic-field-cooled experiments. However, since in our measurements no hysteresis was observed between up- and down-ramping of the magnetic field, these results are equally valid for magnetic-field-ramped experiments.

In the simulations, the critical current density j_c is determined to be the minimum cur-

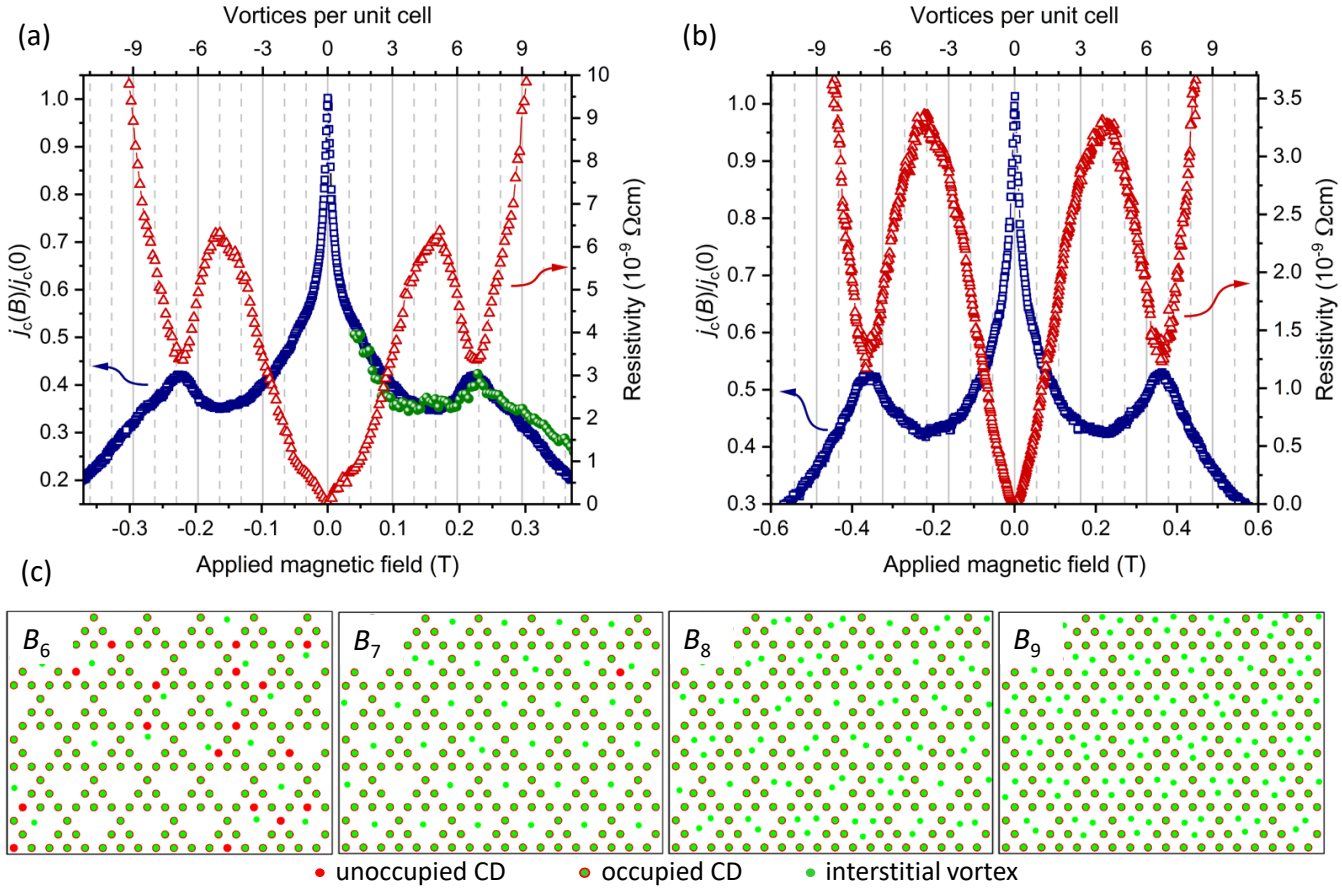


Figure 2: (a) Magnetic field dependence of the normalized critical current at 83 K (blue squares) and resistivity at 83.5 K (red triangles) of a 75 nm thick YBCO film, irradiated with a quasi-kagomé pattern of beam spots (20 nm fwhm) in a HIM (sample QK90). The upper horizontal scale indicates the matching fields B_k, calculated from eq 1, for a filling of the unit cell with k vortices. The peak in the critical current and the minimum in the resistivity correspond to $k = 7$. The green bullets represent the results from molecular dynamics simulations. Only the positive branch of the mirror symmetric results is shown for clarity. (b) Normalized critical current at 52 K (blue squares) and resistivity at 55 K (red triangles) for sample QK70. (c) Simulation of vortex arrangements in the quasi-kagomé lattice of sample QK90 for several applied magnetic fields that correspond to various commensurability conditions as labeled in the graphs. Red circles represent artificial pinning centers and green dots the vortices.

rent density that depins the vortices; in the experiments the common electric field criterion of 10 μV/cm is used. The simulated values for the critical current density are then scaled to the experimental results (for sample QK90) at $B_a = 50$ mT.

The results of the simulations of static vortex configurations at different magnetic fields B_k and for temperatures adapted to the experimental situation are displayed in Figure 2c. For B_6, where the average density of vortices matches the density of CDs, most of the pinning centers are filled with vortices, but several empty pins and, in turn, interstitial vortices can be noticed. This is explained by the strong repulsion between the vortices located on the closely packed pinning sites such that some of these vortices can depin and move in the voids thus minimizing the energy. For B_7 almost all pins are filled and typically one excess vortex sits in the centers of the voids of the quasi-kagomé lattice. If the magnetic field is further increased, all pins are occupied and the voids host two (B_8) or three (B_9) vortices

with minor fluctuations ±1 in this number. In the latter case, the hexagonal vortex lattice is mostly recovered. Note that an experimental visualization of the vortex arrangements in ultradense pinning lattices is challenging. Because $\lambda_{L,ab}(T) \gg a$ in our samples, the magnetic fields of the vortices overlap strongly and magnetic force microscopy might not provide enough contrast.

A simulation of the critical current density $j_c(B_a)$ is displayed in Figure 2a. Indeed, there is no peak in $j_c(B_a)$ visible at B_6, and peaks of $j_c(B_a)$ at B_8 and B_9 are hardly noticeable, whereas a pronounced peak at B_7 is found, in excellent agreement with the experimental results. This unconventional commensurability effect can be explained by the competition of the elastic vortex lattice energy, which favors a hexagonal lattice and the semiregular quasi-kagomé pinning potential. At B_6 filling of all CDs with vortices would lead to a maximized pinning force density, but the repulsion between the trapped vortices leads to a significant number of vacancies at the pinning sites and, in turn, mobile interstitial vortices in the kagomé voids that reduce j_c. On the other hand, for B_9, the elastic energy of the vortex lattice is minimized, but pinning is not so efficient due to the larger number of interstitial vortices. Thus, a commensurate arrangement, in which all pinning sites are occupied and one interstitial vortex is caged in the center of the voids appears to be the most stable structure at temperatures near T_c.

The balance between the pinning forces at the CDs and the vortex caging potential can be tuned with temperature. While both increase at lower temperature, the pinning forces at the artificial defect lattice increase more rapidly.[57] To study this behavior on our samples, we performed electric transport measurements at variable T. Figure 3a shows normalized j_c vs B_a curves for sample QK90 at $67\,\mathrm{K} \leq T \leq 85\,\mathrm{K}$. We find that at temperatures $T < 80\,\mathrm{K}$ a second peak of j_c around B_6 emerges, coalescing with the peak at B_7 into a broader feature with $j_c(B_6) > j_c(B_7)$ at even lower temperatures. This is a formidable demonstration of how the vortices "crystallize" into the quasi-kagomé lattice at lower temperatures when the artificial pinning landscape becomes dominant. Figure 3b displays the critical current density j_c at $B = 0$, calculated from the sample's cross section. However, it has to be cautioned that the irradiated sample contains many CDs, and hence a significant volume in the sample does not contribute to the supercurrent, making a comparison to pristine YBCO films inappropriate. The normalized $j_c(B_6)/j_c(0)$ and $j_c(B_7)/j_c(0)$ curves reveal the crossover at $T = 75\,\mathrm{K}$, where pinning at a matching field of six vortices/unit cell becomes more efficient.

Our findings may be compared to somewhat related simulation results. For a honeycomb pinning lattice it has been demonstrated[41] that j_c of a commensurable vortex arrangement with an additional caged vortex can be larger than that with the pinning sites occupied only. However, this only applies to shallow pinning potentials, whereas the situation is reversed for strong pinning, in excellent accordance with our observation of the crossover to $j_c(B_6) > j_c(B_7)$ at lower temperatures. Note, however, that one caged vortex in a honeycomb lattice restores the ideal hexagonal vortex lattice, while in our quasi-kagomé lattice one interstitial vortex is still associated with elastic energy of the vortex lattice. Thus, additional simulations with varying pinning potentials in the quasi-kagomé lattice are envisaged.

3 CONCLUSIONS

In summary, we have demonstrated the fabrication of periodic arrays of pinning centers in thin YBCO films with ultranarrow lattice spacings down to 70 nm by irradiation with the defocused beam of a HIM. This technique opens the route to create large arrays of pinning sites with user-defined positions and with a resolution superior to the lithographic techniques. As an example of a complex pinning landscape, the quasi-kagomé pinning lattice exhibits an unconventional commensurability effect, when all pins are occupied by vortices and one interstitial vortex is magnetically caged in each void of the lattice. It has been suggested that such caged vortices can be more easily manipulated

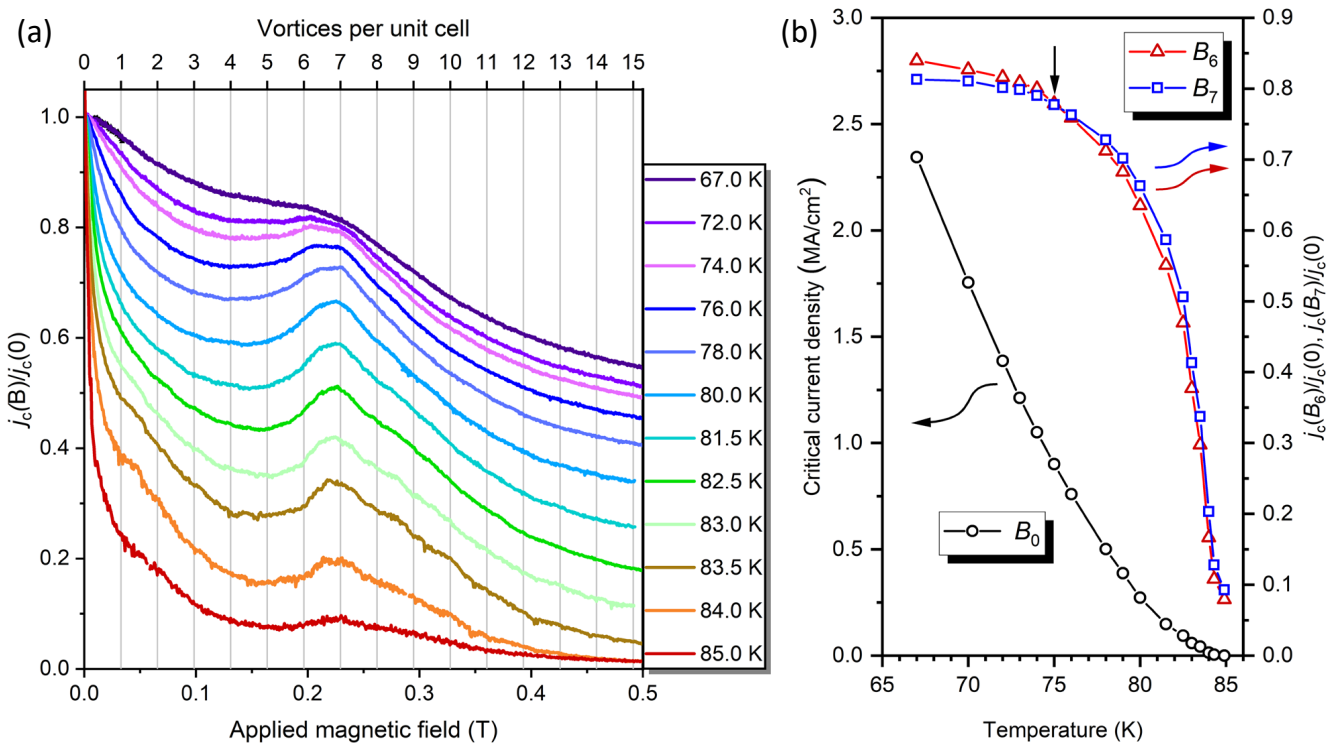


Figure 3: (a) Normalized critical current density of sample QK90 as a function of the applied magnetic field at various temperatures. The branches at reversed polarity of the magnetic field are mirror symmetric and are not shown. The upper horizontal scale displays the commensurability fields for k vortices in the unit cell of the quasi-kagomé pattern. (b) Temperature variation of the critical current density at $B_a = 0$ (black circles) and the normalized critical current densities at B_6 (red triangles) and B_7 (blue squares). At lower temperatures, starting from the crossover at 75 K marked by the arrow, the critical current at the B_6 commensurability field exceeds the critical current at B_7.

along predetermined paths[58] and, hence, our findings can pave the way toward "Fluxonic" applications[59–61] of cuprate superconductors.

4 MATERIALS AND METHODS

Superconducting Film Growth. Thin films of $YBa_2Cu_3O_{7-\delta}$ are grown epitaxially on (100) MgO single-crystal substrates by pulsed-laser deposition using 248 nm KrF-excimer-laser radiation at a fluence of 3.2 J/cm^2. The thicknesses of the films are $t_z = 75 \pm 5$ nm (sample QK90) and $t_z = 50 \pm 5$ nm (sample QK70) as determined by atomic force microscopy. Bridges with dimensions 240×60 μm^2 are lithographically patterned for the electrical transport measurements. Two longitudinal voltage probes with a distance of 100 μm are applied on side arms of the bridges. The as-prepared samples had critical temperatures $T_c \sim 90$ K and transition widths $\Delta T_c \sim 1$ K.

Ion Beam Irradiation. The prepatterned YBCO microbridges are introduced into the Zeiss Orion NanoFab He ion microscope and with low ion fluence the proper alignment of the sample surface to the focus plane of the ion optics is checked. Controlled defocus is achieved by changing the working distance by 8 μm from the focus plane, resulting in irradiation spots of about 20 nm diameter. Every point of the lattice, defined by a deflection list loaded into the Nano Patterning and Visualization Engine (NPVE), is irradiated with 30 keV He^+ ions with a dwell time of 1.2 ms (0.83 ms) and a beam current of 2.0 pA (2.9 pA) for sample QK90 (QK70), corresponding to 15000 He^+ ions/point. The average fluence hitting the sample's surface in the focus spot of about

20 nm fwhm is $4.8 \times 10^{15}\,\mathrm{cm}^{-2}$. The irradiated area is approximately $200\,\mu\mathrm{m} \times 100\,\mu\mathrm{m}$.

Electrical Transport Measurements. The electrical measurements are performed in a closed-cycle cryocooler mounted between the pole pieces of an electromagnet. A Cernox resistor[62] together with a LakeShore 336 temperature controller is used for in-field temperature control to a stability of about 1 mK. The magnetic field, oriented perpendicular to the sample surface, is tuned by a programmable constant current source and measured with a LakeShore 475 gaussmeter with a resolution of 0.1 μT, a zero offset $< 10\mu$T, and a reading accuracy < 0.1 %. The resistivity measurements are performed with a current of 0.8 mA, generated by a Keithley 6221 constant-current source in both polarities to exclude thermoelectric signals, and the voltage is measured with a Keithley 2182A nanovoltmeter. The critical current is determined from isothermal current-voltage ($I-V$) measurements with a voltage criterion of 100 nV, corresponding to $10\,\mu$V/cm. The $I-V$ curves do not exhibit features that could be used to discriminate between the depinning of the vortices trapped in the CDs and the interstitial vortices, respectively.

Numerical Simulations. The simulations are performed in a 2D (in the xy-plane) simulation cell with periodic boundary conditions that models an infinite superconducting film characterized by the penetration depth λ, which is set to $\lambda_{L,ab}(T)$ at finite T. The cell is chosen large enough to avoid finite-size effects. Simulated annealing calculations are performed by numerically integrating the overdamped equations of motion:[39,40,55] $\eta \mathbf{v}_i = \mathbf{f}_i = \mathbf{f}_i^{vv} + \mathbf{f}_i^{vp} + \mathbf{f}_i^{T} + \mathbf{f}_i^{d}$. Here $\mathbf{f}_i$ is the total force per unit length acting on vortex i, $\mathbf{f}_i^{vv}$ and $\mathbf{f}_i^{vp}$ are the forces due to vortex-vortex and vortex-pin interactions, respectively, $\mathbf{f}_i^{T}$ is the thermal stochastic force, and $\mathbf{f}_i^{d}$ is the driving force; η is the viscosity, which is set to unity. The force due to the vortex-vortex interaction is $\mathbf{f}_i^{vv} = \sum_j^{N_v} f_0\, K_1(\mid \mathbf{r}_i - \mathbf{r}_j \mid /\lambda)\, \hat{\mathbf{r}}_{ij}$, where N_v is the number of vortices, K_1 is a modified Bessel function, $\hat{\mathbf{r}}_{ij} = (\mathbf{r}_i - \mathbf{r}_j)/\mid \mathbf{r}_i - \mathbf{r}_j \mid$, and $f_0 = \Phi_0^2/8\pi^2\lambda^3$. The pinning force is $\mathbf{f}_i^{vp} = \sum_k^{N_p} f_p \left(\mid \mathbf{r}_i - \mathbf{r}_k^{(p)} \mid /r_p\right) \Theta\left[\left(r_p - \mid \mathbf{r}_i - \mathbf{r}_k^{(p)} \mid\right)/\lambda\right] \hat{\mathbf{r}}_{ik}^{(p)}$, where N_p is the number of pinning sites, f_p (expressed in f_0) is the maximum pinning force of each short-range parabolic potential well located at $\mathbf{r}_k^{(p)}$, r_p is the range of the pinning potential, Θ is the Heaviside step function, and $\hat{\mathbf{r}}_{ik}^{(p)} = (\mathbf{r}_i - \mathbf{r}_k^{(p)})/\mid \mathbf{r}_i - \mathbf{r}_k^{(p)} \mid$. All the lengths (fields) are expressed in units of λ (Φ_0/λ^2). The ground state of a system of moving vortices is obtained by simulating field-cooled experiments. In this approximation of deep short-range (δ-like) potential wells, the critical current can be defined as follows[39,40,43,44,55] (giving essentially the same results as those obtained using the threshold criterion in dynamical simulations[39,40]): $j_c(\Phi) = j_0 N_v^{(p)}(\Phi)/N_v(\Phi)$, where j_0 is a constant, and study the dimensionless value $J_c = j_c/j_0$.

ASSOCIATED CONTENT

Supporting Information

The Supporting Information is available free of charge on the ACS Publications website at DOI: 10.1021/acsanm.9b01006

> Critical current and resistance data of a square array of vortex pinning centers fabricated by irradiation in the helium ion microscope (PDF)

AUTHOR INFORMATION

Corresponding Author

*E-mail: wolfgang.lang@univie.ac.at

ORCID

Bernd Aichner: 0000-0002-9976-9877
Vyachelav R. Misko: 0000-0002-5290-412X
Meirzhan Dosmailov: 0000-0003-3672-0619
Johannes D. Pedarnig: 0000-0002-7842-3922
Franco Nori: 0000-0003-3682-7432
Wolfgang Lang: 0000-0001-8722-2674

Present Address

M.D.: Al-Farabi Kazakh National University, Almaty, Kazakhstan

Notes

The authors declare no competing financial interest.

ACKNOWLEDGMENTS

The authors thank John Notte and Jason Huang for enlightening discussions on helium ion microscopy and for initial test irradiations in the HIM at Carl Zeiss Ion Microscopy Innovation Center in Peabody, USA, and Georg Zechner for experimental support. B.M. acknowledges funding by the German Academic Scholarship Foundation. V.R.M. and F.N. acknowledge support by the Research Foundation-Flanders (FWO-Vl) and Japan Society for the Promotion of Science (JSPS) (JSPS-FWO Grant VS.059.18N). F.N. is supported in part by the MURI Center for Dynamic Magneto-Optics via the Air Force Office of Scientifc Research (AFOSR) (FA9550-14-1-0040), Army Research Office (ARO) (Grant 73315PH), Asian Office of Aerospace Research and Development (AOARD) (Grant FA2386-18-1-4045), Japan Science and Technology Agency (JST) (the Q-LEAP program and CREST Grant JPMJCR1676), Japan Society for the Promotion of Science (JSPS) (JSPS-RFBR Grant 17-52-50023), RIKEN-AIST Challenge Research Fund. Research was conducted within the framework of the COST Action CA16218 (NANOCOHYBRI) of the European Cooperation in Science and Technology.

REFERENCES

(1) Kleiner, R.; Buckel, W. *Superconductivity*, 3rd ed.; Wiley-VCH: Weinheim, 2016.

(2) Civale, L. Vortex pinning and creep in high-temperature superconductors with columnar defects. *Supercond. Sci. Technol.* **1997**, *10*, A11–A28.

(3) Haugan, T.; Barnes, P. N.; Wheeler, R.; Meisenkothen, F.; Sumption, M. Addition of nanoparticle dispersions to enhance flux pinning of the $YBa_2Cu_3O_{7-x}$ superconductor. *Nature* **2004**, *430*, 867.

(4) Sefrioui, Z.; Arias, D.; González, E. M.; Léon, C.; Santamaria, J.; Vicent, J. L. Vortex liquid entanglement in irradiated $YBa_2Cu_3O_{7-\delta}$ thin films. *Phys. Rev. B* **2001**, *63*, 064503.

(5) Lang, W.; Enzenhofer, T.; Peruzzi, M.; Pedarnig, J. D.; Bäuerle, D.; Horner, C.; Cekan, E.; Platzgummer, E.; Loeschner, H. Tailoring the transport properties of $YBa_2Cu_3O_{7-\delta}$ thin films by light-ion irradiation. *Inst. Phys. Conf. Ser.* **2004**, *181*, 1549–1555.

(6) Cybart, S. A.; Yen, P. X. T.; Cho, E. Y.; Huh, J. U.; Glyantsev, V. N.; Yung, C. S.; Moeckly, B.; Beeman, J. W.; Dynes, R. C. Comparison of YâĂŞBaâĂŞCuâĂŞO Films Irradiated With Helium and Neon Ions for the Fabrication of Josephson Devices. *IEEE Trans. Appl. Supercond.* **2014**, *24*, 1–5.

(7) Lang, W.; Dineva, M.; Marksteiner, M.; Enzenhofer, T.; Siraj, K.; Peruzzi, M.; Pedarnig, J. D.; Bäuerle, D.; Korntner, R.; Cekan, E.; Platzgummer, E.; Loeschner, H. Ion-beam direct-structuring of high-temperature superconductors. *Microelectron. Eng.* **2006**, *83*, 1495–1498.

(8) Lang, W.; Richter, H.; Marksteiner, M.; Siraj, K.; Bodea, M. A.; Pedarnig, J. D.; Grigoropoulos, C.; Bäuerle, D.; Hasenfuss, C.; Palmetshofer, L.; Kolarova, R.; Bauer, P. Masked ion beam irradiation of high-temperature superconductors: patterning of nano-size regions with high point-defect density. *Int. J. Nanotechnol.* **2009**, *6*, 704–14.

(9) Pedarnig, J. D.; Siraj, K.; Bodea, M. A.; Puica, I.; Lang, W.; Kolarova, R.; Bauer, P.; Haselgrübler, K.; Hasenfuss, C.; Beinik, I.; Teichert, C. Surface planarization and masked ion-beam structuring of $YBa_2Cu_3O_7$ thin films. *Thin Solid Films* **2010**, *518*, 7075–80.

(10) Swiecicki, I.; Ulysse, C.; Wolf, T.; Bernard, R.; Bergeal, N.; Briatico, J.; Faini, G.; Lesueur, J.; Villegas, J. E. Strong field-matching effects in superconducting $YBa_2Cu_3O_{7-\delta}$ films with vortex energy landscapes engineered via masked ion irradiation. *Phys. Rev. B* **2012**, *85*, 224502.

(11) Trastoy, J.; Rouco, V.; Ulysse, C.; Bernard, R.; Palau, A.; Puig, T.; Faini, G.; Lesueur, J.; Briatico, J.; Villegas, J. E. Unusual magnetotransport of $YBa_2Cu_3O_{7-\delta}$ films due to the interplay of anisotropy, random disorder and nanoscale periodic pinning. *New J. Phys.* **2013**, *15*, 103022.

(12) Haag, L. T.; Zechner, G.; Lang, W.; Dosmailov, M.; Bodea, M. A.; Pedarnig, J. D. Strong vortex matching effects in YBCO films with periodic modulations of the superconducting order parameter fabricated by masked ion irradiation. *Physica C* **2014**, *503*, 75–81.

(13) Zechner, G.; Jausner, F.; Haag, L. T.; Lang, W.; Dosmailov, M.; Bodea, M. A.; Pedarnig, J. D. Hysteretic Vortex-Matching Effects in High-T_c Superconductors with Nanoscale Periodic Pinning

Landscapes Fabricated by He Ion-Beam Projection. *Phys. Rev. Applied* **2017**, *8*, 014021.

(14) Yang, C. et al. Quantum coherence across bosonic superconductor-anomalous metal-insulator transitions. *arXiv:1901.07706 [cond-mat.supr-con]* **2019**,

(15) Moshchalkov, V. V.; Fritzsche, J. *Nanostructured superconductors*; World Scientific: Singapore, 2011.

(16) Welp, U.; Xiao, Z. L.; Jiang, J. S.; Vlasko-Vlasov, V. K.; Bader, S. D.; Crabtree, G. W.; Liang, J.; Chik, H.; Xu, J. M. Superconducting transition and vortex pinning in Nb films patterned with nanoscale hole arrays. *Phys. Rev. B* **2002**, *66*, 212507.

(17) Hallet, X.; MátéfiâĂŘTempfli, M.; Michotte, S.; Piraux, L.; Vanacken, J.; Moshchalkov, V. V.; MátéfiâĂŘTempfli, S. Quasi-Hexagonal Vortex-Pinning Lattice Using Anodized Aluminum Oxide Nanotemplates. *Small* **2009**, *5*, 2413–2416.

(18) Wölbing, R.; Schwarz, T.; Müller, B.; Nagel, J.; Kemmler, M.; Kleiner, R.; Koelle, D. Optimizing the spin sensitivity of grain boundary junction nanoSQUIDs – towards detection of small spin systems with single-spin resolution. *Supercond. Sci. Technol.* **2014**, *27*, 125007.

(19) Thiel, L.; Rohner, D.; Ganzhorn, M.; Appel, P.; Neu, E.; Müller, B.; Kleiner, R.; Koelle, D.; Maletinsky, P. Quantitative nanoscale vortex imaging using a cryogenic quantum magnetometer. *Nat. Nanotechnol.* **2016**, *11*, 677–681.

(20) Martínez-Pérez, M. J.; Müller, B.; Schwebius, D.; Korinski, D.; Kleiner, R.; Sesé, J.; Koelle, D. NanoSQUID magnetometry of individual cobalt nanoparticles grown by focused electron beam induced deposition. *Supercond. Sci. Technol. – focus issue on NanoSQUIDs and their applications* **2017**, *30*, 024003.

(21) Rohner, D.; Thiel, L.; Müller, B.; Kasperczyk, M.; Kleiner, R.; Koelle, D.; Maletinsky, P. Real-space probing of the local magnetic response of thin-film superconductors using single spin magnetometry. *Sensors* **2018**, *18*, 3790.

(22) Dam, B.; Huijbregtse, J. M.; Klaassen, F. C.; van der Geest, R. C. F.; Doornbos, G.; Rector, J. H.; Testa, A. M.; Freisem, S.; Martinez, J. C.; Stäuble-Pümpin, B.; Griessen, R. Origin of high critical currents in $YBa_2Cu_3O_{7-\delta}$ superconducting thin films. *Nature* **1999**, *399*, 439–442.

(23) Castellanos, A.; Wördenweber, R.; Ockenfuss, G.; v.d. Hart, A.; Keck, K. Preparation of regular arrays of antidots in $YBa_2Cu_3O_7$ thin films and observation of vortex lattice matching effects. *Appl. Phys. Lett.* **1997**, *71*, 962–964.

(24) https://www.zeiss.com/microscopy/int/products/multiple-ion-beam/orion-nanofab-for-materials.html. 2019-05-17.

(25) Ward, B. W.; Notte, J. A.; Economou, N. P. Helium ion microscope: A new tool for nanoscale microscopy and metrology. *Journal of Vacuum Science & Technology B* **2006**, *24*, 2871–2874.

(26) Hlawacek, G., Gölzhäuser, A., Eds. *Helium Ion Microscopy*; Springer International Publishing: Switzerland, 2016.

(27) Flatabø, R.; Agarwal, A.; Hobbs, R.; Greve, M. M.; Holst, B.; Berggren, K. K. Exploring proximity effects and large depth of field in helium ion beam lithography: large-area dense patterns and tilted surface exposure. *Nanotechnology* **2018**, *29*, 275301.

(28) Emmrich, D.; Beyer, A.; Nadzeyka, A.; Bauerdick, S.; Meyer, J. C.; Kotakoski, J.; Gölzhäuser, A. Nanopore fabrication and characterization by helium ion microscopy. *Appl. Phys. Lett.* **2016**, *108*, 163103.

(29) Cybart, S. A.; Cho, E. Y.; Wong, T. J.; Wehlin, B. H.; Ma, M. K.; Huynh, C.; Dynes, R. C. Nano Josephson superconducting tunnel junctions in $YBa_2Cu_3O_{7-\delta}$ directly patterned with a focused helium ion beam. *Nat. Nanotechnol.* **2015**, *10*, 598.

(30) Cho, E. Y.; Ma, M. K.; Huynh, C.; Pratt, K.; Paulson, D. N.; Glyantsev, V. N.; Dynes, R. C.; Cybart, S. A. $YBa_2Cu_3O_{7-\delta}$ superconducting quantum interference devices with metallic to insulating barriers written with a focused helium ion beam. *Appl. Phys. Lett.* **2015**, *106*, 252601.

(31) Cho, E. Y.; Zhou, Y. W.; Cho, J. Y.; Cybart, S. A. Superconducting nano Josephson junctions patterned with a focused helium ion beam. *Appl. Phys. Lett.* **2018**, *113*, 022604.

(32) Müller, B.; Karrer, M.; Limberger, F.; Becker, M.; Schröppel, B.; Burkhardt, C. J.; Kleiner, R.; Goldobin, E.; Koelle, D. Josephson Junctions and SQUIDs Created by Focused Helium-Ion-Beam Irradiation of $YBa_2Cu_3O_7$. *Phys. Rev. Applied* **2019**, *11*, 044082.

(33) Sekirnjak, C.; Lang, W.; Proyer, S.; Schwab, P. Novel approach for the analysis of the fluctuation magnetoconductivity in $YBa_2Cu_3O_7$ thin films. *Physica C* **1995**, *243*, 60–68.

(34) Ziegler, J. F.; Ziegler, M. D.; Biersack, J. P. SRIM âĂŞ The stopping and range of ions in matter (2010). *Nucl. Instrum. Methods Phys. Res., Sect. B* **2010**, *268*, 1818–23.

(35) Mletschnig, K. L.; Lang, W. Nano-patterning of cuprate superconductors by masked He^+ ion irradiation: 3-dimensional profiles of the local critical temperature. *Microelectron. Eng.* **2019**, *215*, 110982.

(36) Niebieskikwiat, D.; Silhanek, A.; Civale, L.; Nieva, G.; Levy, P.; Krusin-Elbaum, L. Suppression of matching field effects by splay and pinning energy dispersion in $YBa_2Cu_3O_7$ with columnar defects. *Phys. Rev. B* **2001**, *63*, 144504.

(37) Ooi, S.; Mochiku, T.; Yu, S.; Sadki, E. S.; Hirata, K. Matching effect of vortex lattice in $Bi_2Sr_2CaCu_2O_{8+y}$ with artificial periodic defects. *Physica C* **2005**, *426*, 113–117.

(38) Laguna, M. F.; Balseiro, C. A.; Domínguez, D.; Nori, F. Vortex structure and dynamics in kagomé and triangular pinning potentials. *Phys. Rev. B* **2001**, *64*, 104505.

(39) Misko, V.; Savel'ev, S.; Nori, F. Critical Currents in Quasiperiodic Pinning Arrays: Chains and Penrose Lattices. *Phys. Rev. Lett.* **2005**, *95*, 177007.

(40) Misko, V. R.; Savel'ev, S.; Nori, F. Critical currents in superconductors with quasiperiodic pinning arrays: One-dimensional chains and two-dimensional Penrose lattices. *Phys. Rev. B* **2006**, *74*, 024522.

(41) Reichhardt, C.; Olson Reichhardt, C. J. Vortex molecular crystal and vortex plastic crystal states in honeycomb and kagomé pinning arrays. *Phys. Rev. B* **2007**, *76*, 064523.

(42) Kemmler, M.; Gürlich, C.; Sterck, A.; Pöhler, H.; Neuhaus, M.; Siegel, M.; Kleiner, R.; Koelle, D. Commensurability effects in superconducting Nb films with quasiperiodic pinning arrays. *Phys. Rev. Lett.* **2006**, *97*, 147003.

(43) Misko, V. R.; Bothner, D.; Kemmler, M.; Kleiner, R.; Koelle, D.; Peeters, F. M.; Nori, F. Enhancing the critical current in quasiperiodic pinning arrays below and above the matching magnetic flux. *Phys. Rev. B* **2010**, *82*, 184512.

(44) Bothner, D.; Seidl, R.; Misko, V. R.; Kleiner, R.; Koelle, D.; Kemmler, M. Unusual commensurability effects in quasiperiodic pinning arrays induced by local inhomogeneities of the pinning site density. *Supercond. Sci. Technol.* **2014**, *27*, 065002.

(45) Villegas, J. E.; Montero, M. I.; Li, C.-P.; Schuller, I. K. Correlation length of quasiperiodic vortex lattices. *Phys. Rev. Lett.* **2006**, *97*, 027002.

(46) Silhanek, A. V.; Gillijns, W.; Moshchalkov, V. V.; Zhu, B. Y.; Moonens, J.; Leunissen, L. H. A. Enhanced pinning and proliferation of matching effects in a superconducting film with a Penrose array of magnetic dots. *Appl. Phys. Lett.* **2006**, *89*, 152507.

(47) Kramer, R. B. G.; Silhanek, A. V.; Van de Vondel, J.; Raes, B.; Moshchalkov, V. V. Symmetry-Induced Giant Vortex State in a Superconducting Pb Film with a Fivefold Penrose Array of Magnetic Pinning Centers. *Phys. Rev. Lett.* **2009**, *103*, 067007.

(48) Perez de Lara, D.; Alija, A.; Gonzalez, E. M.; Velez, M.; Martin, J. I.; Vicent, J. L. Vortex ratchet reversal at fractional matching fields in kagomélike array with symmetric pinning centers. *Phys. Rev. B* **2010**, *82*, 174503.

(49) Latimer, M. L.; Berdiyorov, G. R.; Xiao, Z. L.; Kwok, W. K.; Peeters, F. M. Vortex interaction enhanced saturation number and caging effect in a superconducting film with a honeycomb array of nanoscale holes. *Phys. Rev. B* **2012**, *85*, 012505.

(50) Cuppens, J.; Ataklti, G. W.; Gillijns, W.; Van de Vondel, J.; Moshchalkov, V. V.; Silhanek, A. V. Vortex Dynamics in a Superconducting Film with a Kagome andÂăaÂăHoneycomb Pinning Landscape. *J. Supercond. Novel Magn.* **2011**, *24*, 7–11.

(51) Libál, A.; Olson Reichhardt, C. J.; Reichhardt, C. Creating artificial ice states using vortices in nanostructured superconductors. *Phys. Rev. Lett.* **2009**, *102*, 237004.

(52) Latimer, M. L.; Berdiyorov, G. R.; Xiao, Z. L.; Peeters, F. M.; Kwok, W. K. Realization of Artificial Ice Systems for Magnetic Vortices in a Superconducting MoGe Thin Film with Patterned Nanostructures. *Phys. Rev. Lett.* **2013**, *111*, 067001.

(53) Xue, C.; Ge, J.-Y.; He, A.; Zharinov, V. S.; Moshchalkov, V. V.; Zhou, Y. H.; Silhanek, A. V.; Van de Vondel, J. Tunable artificial vortex ice in nanostructured superconductors with a frustrated kagome lattice of paired antidots. *Phys. Rev. B* **2018**, *97*, 134506.

(54) Trastoy, J.; Malnou, M.; Ulysse, C.; Bernard, R.; Bergeal, N.; Faini, G.; Lesueur, J.; Briatico, J.; Villegas, J. E. Freezing and thawing of artificial ice by thermal switching of geometric frustration in magnetic flux lattices. *Nat. Nanotechnol.* **2014**, *9*, 710–715.

(55) Reichhardt, C.; Olson, C. J.; Nori, F. Commensurate and incommensurate vortex states in superconductors with periodic pinning arrays. *Phys. Rev. B* **1998**, *57*, 7937–7943.

(56) Misko, V. R.; Nori, F. Magnetic flux pinning in superconductors with hyperbolic-tessellation arrays of pinning sites. *Phys. Rev. B* **2012**, *85*, 184506.

(57) Khalfin, I. B.; Shapiro, B. Y. Relaxation of magnetic flux in a superconductor with a system of columnar defects. *Physica C* **1993**, *207*, 359–365.

(58) Togawa, Y.; Harada, K.; Akashi, T.; Kasai, H.; Matsuda, T.; Nori, F.; Maeda, A.; Tonomura, A. Direct Observation of Rectified Motion of Vortices in a Niobium Superconductor. *Phys. Rev. Lett.* **2005**, *95*, 087002.

(59) Wambaugh, J. F.; Reichhardt, C.; Olson, C. J.; Marchesoni, F.; Nori, F. Superconducting fluxon pumps and lenses. *Phys. Rev. Lett.* **1999**, *83*, 5106–5109.

(60) Hastings, M. B.; Olson Reichhardt, C. J.; Reichhardt, C. Ratchet cellular automata. *Phys. Rev. Lett.* **2003**, *90*, 247004.

(61) Milošević, M. V.; Berdiyorov, G. R.; Peeters, F. M. Fluxonic cellular automata. *Appl. Phys. Lett.* **2007**, *91*, 212501.

(62) Heine, G.; Lang, W. Magnetoresistance of the new ceramic 'Cernox' thermometer from 4.2 K to 300 K in magnetic fields up to 13 T. *Cryogenics* **1998**, *38*, 377–379.